

Monte Carlo Simulation of the Photon-Tagger Focal-Plane Electronics at the MAX IV Laboratory

L. S. Myers^{a,1}, G. Feldman^b, K. G. Fissum^{c,*}, L. Isaksson^f, M. A. Kovash^d,
A. M. Nathan^a, R. E. Pywell^e, B. Schröder^f

^aUniversity of Illinois at Urbana-Champaign, Urbana-Champaign IL 61802, USA

^bThe George Washington University, Washington DC 20052, USA

^cLund University, SE-221 00 Lund, Sweden

^dUniversity of Kentucky, Lexington KY 40506, USA

^eUniversity of Saskatchewan, Saskatoon SK Canada S7N 5E2

^fMAX IV Laboratory, Lund University, SE-221 00 Lund, Sweden

Abstract

Rate-dependent effects in the electronics used to instrument the tagger focal plane at the MAX IV Laboratory have been investigated using the novel approach of Monte Carlo simulation. Results are compared to analytical calculations as well as experimental data for both specialized testing and production running to demonstrate a thorough understanding of the behavior of the detector system.

Keywords: tagger hodoscope, electronics simulation, rate dependencies

PACS: 29.90.+r

1. Introduction

The MAX IV Laboratory [1] is the Swedish National Electron Accelerator Facility located in Lund, Sweden. The Tagged-Photon Facility (TPF) at the MAX IV Laboratory [2, 3] is the beamline at the facility which utilizes the 200 MeV pulse-stretcher mode [4]. Electrons in pulses with widths of about 200 ns are accelerated to energies up to 200 MeV and then injected into the MAX I pulse-stretcher ring (PSR) at a frequency of 10 Hz. The electrons are then slowly extracted over the following 100 ms, before the arrival of the next pulse from the linac, and then transported to the TPF. In this manner, the pulsed electron beam originating in the injector is converted into a continuous,

*Corresponding author. Telephone: +46 46 222 9677; Fax: +46 46 222 4709
Preprint submitted to Nuclear Instruments and Methods A September 15, 2018
Email address: kevin.fissum@nuclear.lu.se (K. G. Fissum)

¹present address: Duke University, Durham NC 27708, USA

24 but non-uniform, electron beam with an average current of approximately 20 nA.
25 Understanding rate-dependent effects in the experiment electronics resulting
26 from the time structure in the electron beam required the efforts reported upon
27 in this paper.

28 The TPF houses two photon-tagging spectrometers inherited from the Saskatchewan
29 Accelerator Laboratory (SAL) in Saskatoon, Canada [5–7]. These devices are
30 used to perform photonuclear experiments via the well-known photon-tagging
31 technique [8] illustrated in Fig. 1. The electron beam passes through a thin
32 metal radiator ($\sim 100 \mu\text{m Al}$), and a small portion ($\sim 0.1\%$) of the incident elec-
33 tron beam is converted into a bremsstrahlung photon beam. Electrons that do
34 not interact are dumped onto a well-shielded Faraday cup which registers the
35 non-interacting electron-beam current. The resulting bremsstrahlung photon
36 beam passes through a collimator to define its size prior to striking the exper-
37 imental target. Post-bremsstrahlung electrons are momentum-analyzed using
38 one of the magnetic photon-tagging spectrometers together with a 63-counter
39 plastic-scintillator array positioned at the spectrometer focal plane (FP) [2]. A
40 time coincidence between a reaction product from a photon-target interaction
41 and a recoiling electron is a tagged-photon event.

42 The energy of a tagged photon is determined from the difference between the
43 energy of the incident electron beam and the energy of the post-bremsstrahlung
44 electron detected in the focal plane. The number of electrons striking a given
45 channel in the FP array is a crucial experimental parameter, as it is part of
46 the overall experimental photon-flux normalization. The number of electrons
47 must be corrected for the tagging efficiency [9], which measures the probability
48 that the bremsstrahlung photon in question passes through the beam-defining
49 collimator and is incident upon the experimental target.

50 The number of electrons counted in a given FP channel must also be cor-
51 rected for rate-dependent effects. These effects arise due to the fact that the
52 electron beam striking the radiator is not truly continuous, but rather has a
53 periodic structure of varying intensity. These intensity variations are due to the
54 non-uniform filling of the PSR by the injector and the frequency of the shaker

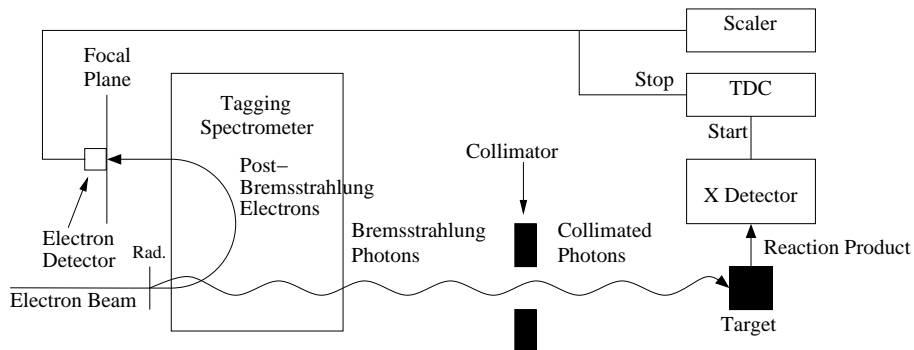


Figure 1: The photon-tagging technique. Beam electrons may radiate bremsstrahlung photons. Post-bremsstrahlung electrons are momentum analyzed using the photon tagger, which consists of a magnetic tagging spectrometer and a FP array of electron detectors. Bremsstrahlung photons which pass through the collimator strike the experiment target and may induce photonuclear reactions which result in a reaction product being detected. The coincidence between a reaction product and a post-bremsstrahlung electron is a tagged-photon event.

55 in the PSR which is used to disturb the electrons from the central orbit of the
 56 ring lattice in the extraction process. The measure of this intensity variation is
 57 the duty factor of the beam [10]. At an operating current of 20 nA, the average
 58 rate in a FP channel is approximately 1 MHz; however, the instantaneous rate
 59 in the same FP channel can be as high as 4 MHz [11] due to the duty fac-
 60 tor. Using this exact tagging spectrometer and FP detector array at such high
 61 rates, Hornidge *et al.* observed substantial rate-dependent effects in deuterium
 62 Compton-scattering data measured at SAL [12, 13]. In order to determine the
 63 necessary rate-dependent corrections, Pywell developed a Monte-Carlo simu-
 64 lation of the tagger setup [14]. This original simulation has been completely
 65 overhauled and adapted to the present experimental conditions of the TPF at
 66 the MAX IV Laboratory.

67 In this paper, we present a detailed comparison between both dedicated
 68 test data and experimental production data obtained using the TPF and the
 69 overhauled Monte Carlo, and we demonstrate a clear understanding of the rate-
 70 dependent effects that we have encountered.

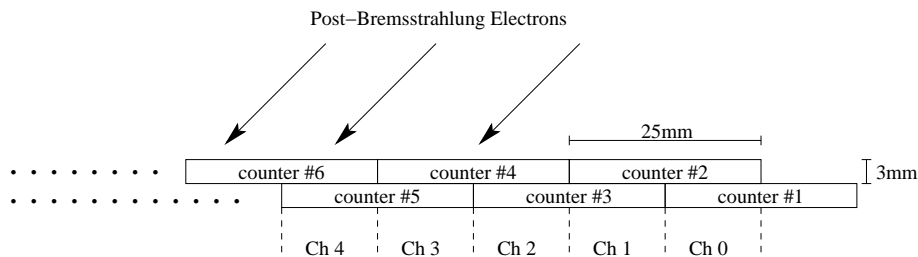


Figure 2: The FP hodoscope in 50%-overlap configuration. A coincidence between a counter in the front plane (even) and a counter in the back plane (odd) defines a tagger channel. There are a total of 63 counters and 62 channels in the focal plane.

71 2. Rate-dependent effects

72 The FP detector hodoscope consists of an array of NE110 scintillators ar-
 73 ranged in two parallel rows of scintillators. The front row nearest the exit win-
 74 dow of the tagger magnet has 31 elements, while the back row has 32 elements.
 75 The relative orientation of the two rows may be varied in order to adjust the
 76 overlap between the rows from complete (100%) to 50% (the configuration used
 77 for this work). By decreasing the overlap, the recoil-electron energy resolution
 78 is increased and consequently the photon-energy resolution is also increased (see
 79 Fig. 2).

80 Each counter is instrumented with a Hamamatsu R1450 photomultiplier
 81 tube with a 19 mm head, and high voltage is supplied by a LeCroy 1440 power
 82 supply. The signals from the FP counters are passed to LRS 4413 leading-edge
 83 discriminators operated in burst-guard mode. These discriminators are used to
 84 generate logic signals of widths varying from 25 ns to 50 ns depending upon the
 85 experiment in question. Coincidences between two overlapping scintillators in
 86 the front and back rows are identified in overlap coincidence modules designed
 87 and built at SAL – it is these coincidences that define tagger channels. When
 88 operated in 50% overlap mode, the length of the hodoscope is 842 mm, and each
 89 of the so-defined tagger channels has a physical width of 13 mm. The logical
 90 OR of the 62 FP channels is used as a trigger for a recoil-electron event (see
 91 Fig. 3). When a recoil-electron trigger occurs in coincidence with a trigger from

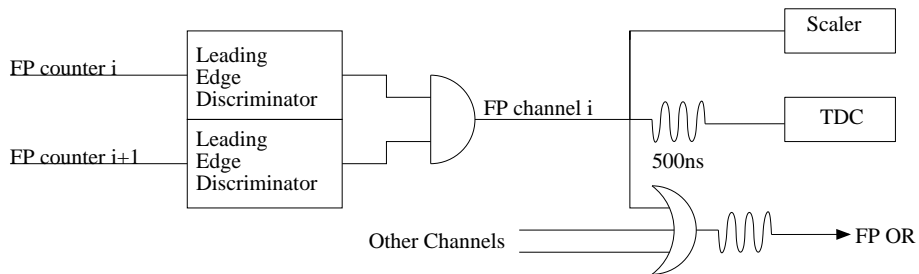


Figure 3: The FP electronics. A coincidence between an electron-detector signal in the front plane and an electron-detector signal in the back plane defines a tagger channel. The coincidence module looking for these overlaps was from SAL. This signal is counted and used to stop a TDC started by the photonuclear reaction-product detector. The logical OR of all the focal-plane channel signals is the FP OR trigger.

92 the experiment detectors, a candidate tagged-photon event is registered.

93 Two advantages to requiring a coincidence between the front and back rows
 94 of scintillators in the FP hodoscope are that the gamma-ray background in the
 95 tagger hall is not registered by the tagger, and that the photon-energy resolution
 96 may be increased by varying the relative orientation of the two scintillator planes
 97 rather than building a new array with smaller scintillators. However, a major
 98 disadvantage of requiring a coincidence between the front and back rows of
 99 scintillators in the FP hodoscope is the creation of so-called “ghost events” at
 100 high rates. The ghosts are an artificial creation of the instrumentation of the
 101 focal plane. The scenario leading to a ghost event is illustrated in the top panel
 102 of Fig. 4. Two electrons strike next-to-neighboring channels (counters F1 · B1
 103 and F2 · B2) simultaneously which creates the illusion of an electron in the
 104 channel in the middle (counters F1 · B2) – the ghost event. The accidental
 105 coincidences that result in ghost events depend on the electron rate, the width
 106 of the the discriminator output pulses, and the resolving time of the coincidence
 107 modules. Because these ghosts are formed in the FP electronics, the accidental
 108 coincidences are registered in both the scalers and the TDC modules. This
 109 results in a partial cancellation of the effect. Understanding the dependence of
 110 the ghosts on the input conditions and determining the amount of cancellation

111 requires a Monte Carlo simulation of the tagger setup and electronics.

112 High recoil-electron rates can also lead to real electron stops being missed by
113 the leading-edge discriminators (even though they are operated in burst-guard
114 mode) and the overlap coincidence modules due to dead-time effects. They
115 also result in asymmetries in the data acquisition, since the scalers counting
116 the electron signals which are used to normalize the data are much faster than
117 the TDCs which identify tagged-photon events – see Sect. 4.1. And finally,
118 when single-hit TDCs are employed, a random electron may be detected in the
119 FP channel before the actual electron that corresponds to the tagged photon.
120 The result is that the single-hit TDC stops too early, leading to a well-studied
121 phenomenon known as stolen coincidences [15] – see Fig. 5.

122 In order to measure the number of stolen coincidences in the data set, a
123 prescaled FP (pFP) trigger is routinely included in the data stream – see Fig. 6.
124 To form this trigger, a representative logic signal from a single FP channel
125 is passed to a bank of three scalers (uninhibited, bad-beam inhibited², and
126 bad-beam OR busy DAQ inhibited). A fourth copy of this signal is bad-beam
127 inhibited, rate-divided (typically by a factor of 10^5), and used as the pFP trigger.
128 It is trickled into the data stream at a rate of ~ 10 Hz as a valid trigger and is used
129 to start the FP TDCs. As a result, for the pFP-triggered subset of events, the FP
130 TDCs are started by the pFP signal and stopped by the usual recoil-electron
131 signal (recall Fig. 3). Note that the coincidence between the normal recoil-
132 electron signals in the front and back scintillator planes was established using
133 SAL modules, while the same coincidence for the pFP trigger was established
134 using a LRS 622.

135 Figure 7 shows a typical TDC spectrum where the start signals were provided
136 by the pFP trigger and the stop signals were provided by recoil electrons striking
137 the focal plane. In the TDC spectrum, we expected to see a single self-timing
138 peak (shown here from channels 165 to 175) and a grouping of events to the left
139 of the self-timing peak (shown here below channel 150) corresponding to stolen

²Bad beam is defined as the first 1 ms of the extracted beam from the PSR.

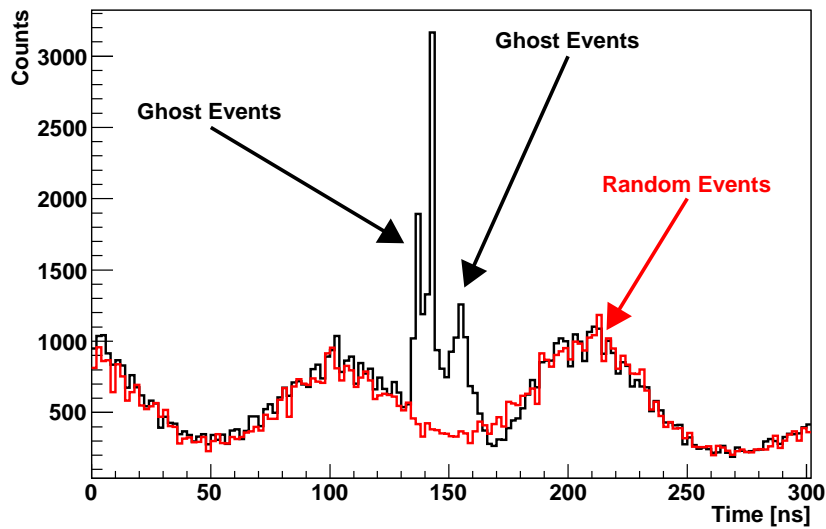
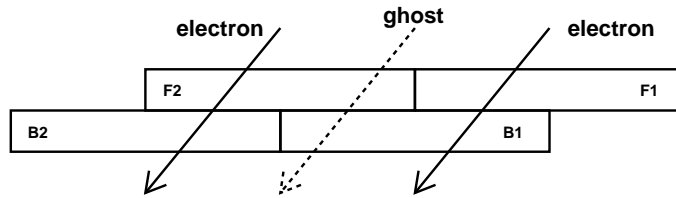


Figure 4: (Color online) (Top) The scenario that leads to a ghost event. Real electrons (solid arrows) in next-neighboring FP channels arrive nearly simultaneously. This creates the illusion – or “ghost” – of an electron (dashed arrows) in the counters that constitute the intermediate FP channel. (Bottom) A demonstration of ghost events within the data. A coincidence between the experiment trigger and FP channel 36 has been required. Adjacent FP channel 37 (black) and physically distant FP channel 40 (red) TDC spectra are shown. Both were started by the same experiment trigger. The red spectrum is thus due to untagged, accidental events. The “ripple” in the accidental distribution is discussed in Sect. 4.2. The black spectrum also shows these untagged, accidental events. In addition, there are three clear peaks between 130 and 170 ns. The sharp, dominant peak is a combination of accidental coincidences and ghosts. The secondary and tertiary peaks to the left and the right are due to ghost events. The multiple peaks were determined to arise from the pulse-timing characteristics of the TDC (see Sect. 4.1).

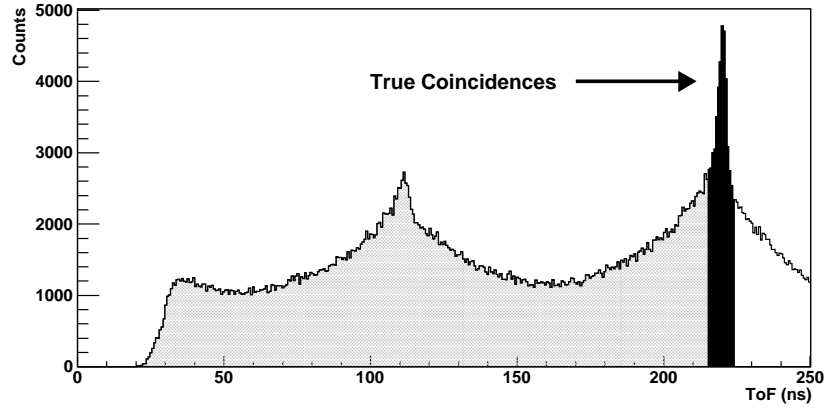


Figure 5: An illustration of the stolen-coincidence effect in a single-hit TDC spectrum acquired at a high post-bremsstrahlung electron rate. The black peak at channel 225 represents true coincidences between the reaction-product detector and the hodoscope. This point in time is the earliest possible that a true coincidence may be registered. Events in the grey shaded region correspond to random post-bremsstrahlung electrons stopping the FP TDCs before this earliest possible point in time. The true coincidence is thus stolen when a single-hit TDC is used. Note that the “peak” at channel 110 is due to the non-uniform filling of the ring in the extracted electron beam.

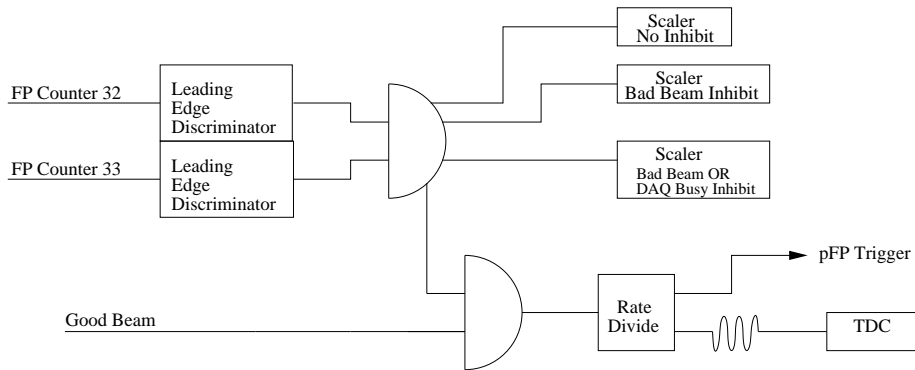


Figure 6: The pFP trigger. The signal from a single FP channel is rate divided to ~ 10 Hz and then passed to the DAQ as a valid event trigger and used to start the FP TDCs.

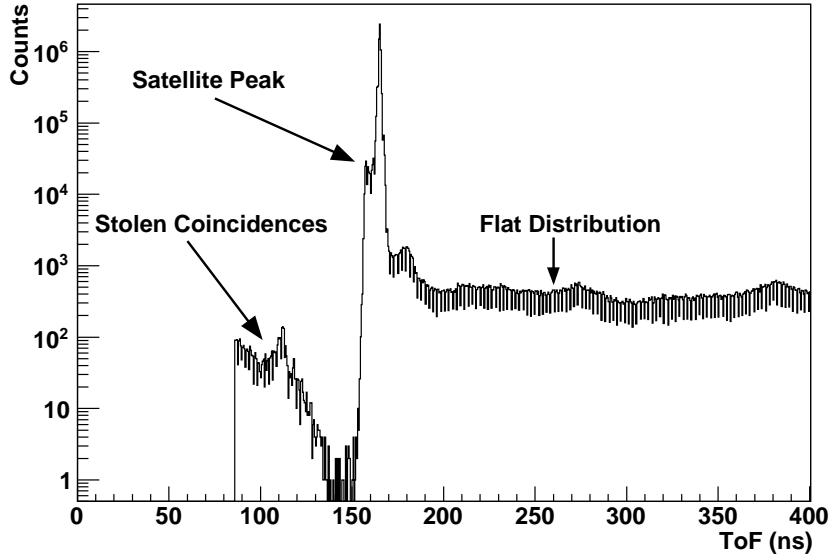


Figure 7: A typical pFP TDC spectrum. A self-timing peak between channels 165 and 175 is clearly evident. The grouping of events below channel 150 are stolen coincidences – see text for details. The satellite peak between channels 150 and 165 as well as the flat distribution of events from channels 180 to 400 and higher could not be explained without the help of the simulation.

140 coincidences. The appearances of a satellite peak (shown here from channels
 141 150 to 165) as well as a flat distribution of events at times greater than the
 142 self-timing peak (events ranging from channel 180 to 400 and higher) were a
 143 mystery prior to the simulation efforts.

144 3. Basic features of the simulation

145 Using the procedure established by Pywell, the Monte Carlo simulation mod-
 146 els the FP electronics in 1 ns steps from the recoil-electron detectors to the
 147 scalers and TDCs, traversing all of the intermediate electronics in the process.
 148 In contrast to the Pywell procedure, our simulation addresses all 62 FP channels
 149 simultaneously. In an effort to make the simulation as versatile as possible, it
 150 was written so that many of the initial conditions are input from separate files

151 rather than being hard-coded. During each ns of the simulation, the FP chan-
152 nels are checked to see if a recoil electron struck the channel. The probability
153 for such an electron event is dependent on the instantaneous electron rate in the
154 FP channel, which in turn depends on the time structure of the electron beam.
155 Both of these parameters are adjustable inputs.

156 A Poisson distribution is used to generate recoil electrons in the FP chan-
157 nels³. If an electron is observed in a given channel, the corresponding counter
158 discriminators are updated, and then the counter discriminator pulses are tracked
159 to the overlap coincidence modules which are updated. The signals from the
160 overlap coincidence modules are then propagated to the FP scalers and TDCs
161 which record the electron. For each recoil electron in a FP channel, there is also
162 a probability that the corresponding photon generates a start for the FP TDCs.
163 The likelihood of this occurring (which is related to the tagging efficiency) is
164 another input to the simulation. Additionally, untagged photons and cosmic-
165 ray events can also be used to start the FP TDCs⁴. If there is an experiment
166 trigger (either a pFP electron, a tagged or untagged photon, or a cosmic ray),
167 the FP TDCs are started and the FP scalers are inhibited. The duration of the
168 inhibit may be adjusted to precisely match the experimental running conditions.
169 Finally, the simulation checks each coincidence in the coincidence modules to
170 see if a corresponding real electron is responsible for generating the coincidence.
171 If no electron was present, then a flag is set which identifies the coincidence
172 output as a ghost event. This flag allows for the analysis of both real and ghost
173 events and leads to the subsequent correction factors for the data.

174 The original code developed at SAL by Pywell was written in FORTRAN.
175 The new simulation was updated to C++ and was compiled with gcc, and
176 the simulation output is written to a ROOT file [17]. The compiled code is
177 run on a 2.66 GHz CPU which takes approximately one hour to simulate the

³ The individual FP counter rates were not recorded.

⁴ The corresponding count rate is used to generate a random event using a Poisson distribution.

178 FP electronics for events spanning a time interval of one second. A flow chart
179 describing the simulation is shown in Fig. 8, and a summary of input parameters
180 is presented in Table 1. Most of the inputs to the simulation listed in Table 1
181 are taken directly from the electronics setup (such as pulse widths) or from the
182 data itself (such as electron rates and tagging efficiency).

183 **4. Input parameters**

184 *4.1. Electronics*

185 Once the framework of the tagger simulation was developed, it was nec-
186 essary to understand the response of the various electronics modules in order
187 to implement them correctly. This required a thorough understanding of the
188 leading-edge discriminators, various coincidence modules, TDCs, and scalers.

189 As previously mentioned, the LRS 4413 leading-edge discriminators used to
190 instrument the focal plane were operated in burst-guard mode, which resulted in
191 behavior that was especially important at high rates. The modules are designed
192 to produce an output pulse of a fixed, user-determined width when the threshold
193 is crossed. If a second event arrives at the discriminator before the end of the
194 previous output pulse, the output will be updated and will extend to the greater
195 of the fixed width or the threshold re-crossing of the second input pulse. Any
196 subsequent inputs will be ignored until the fixed width has passed and the
197 discriminator is reset.

198 Figure 9 illustrates the burst-guard behavior of the LRS 4413 leading-edge
199 discriminator. In panel (a), a single analog signal corresponding to an electron
200 is discriminated, resulting in a 40 ns output pulse. Panels (b) and (c) show the
201 conditions for updating the output pulse with a second electron. In panel (b),
202 the re-crossing associated with the second electron occurs before the original
203 output ends – the output pulse is thus the same as in panel (a), and the second
204 electron is missed. In panel (c), the second re-crossing occurs after the output
205 would have ended, so the duration of the output signal is extended. Third hits
206 are never registered, as shown in panel (d).

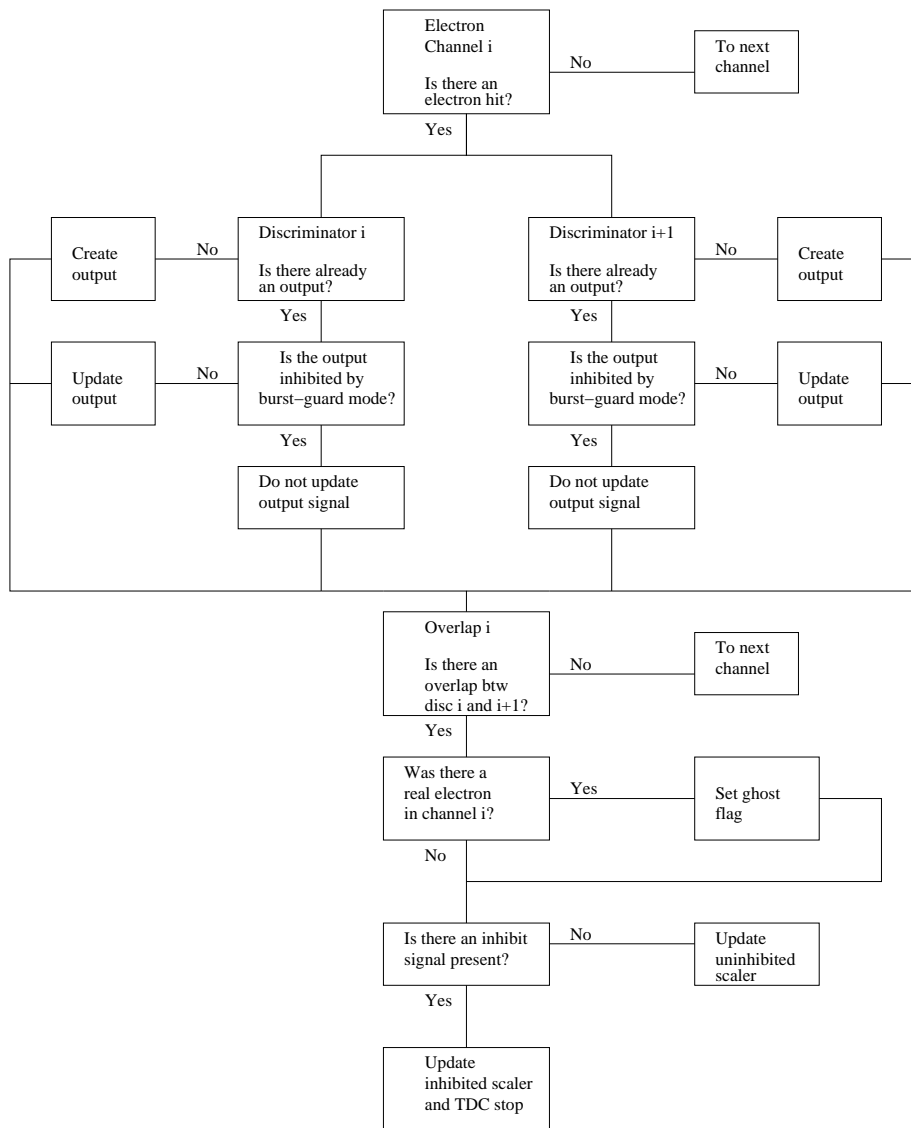


Figure 8: Flowchart describing the simulation. See text for details.

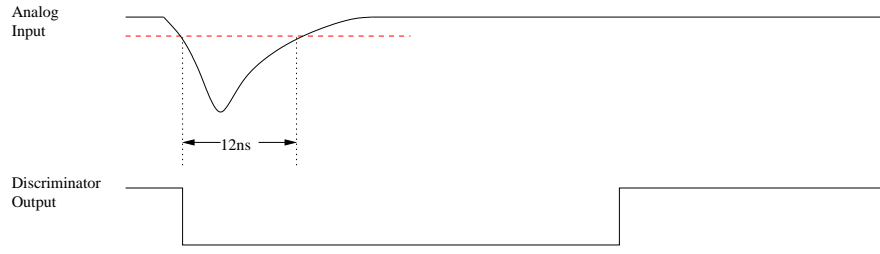


Figure 1(a)

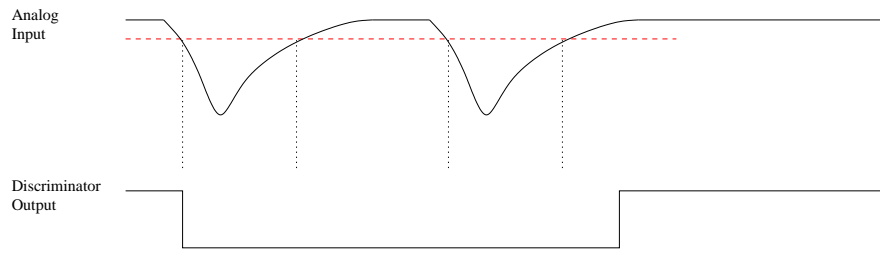


Figure 1(b)

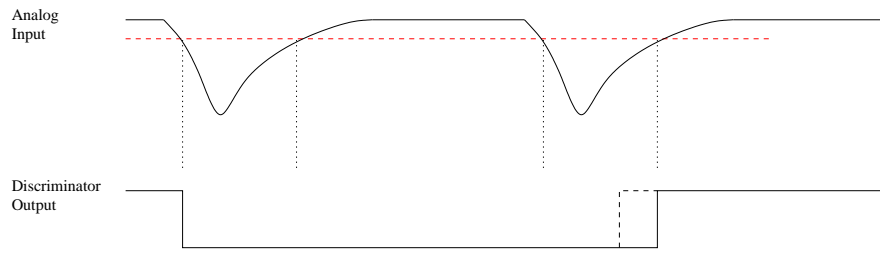


Figure 1(c)

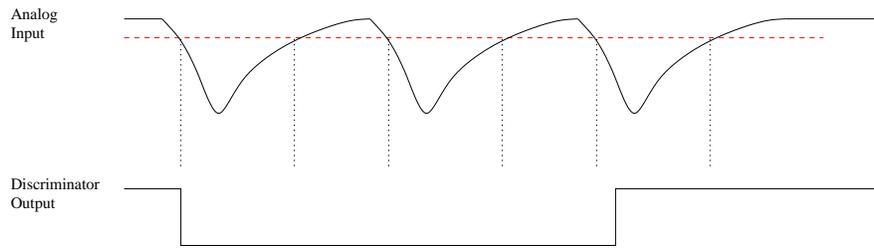


Figure 1(d)

Figure 9: An illustration of the behavior of the LRS 4413 leading-edge discriminators operating in burst-guard mode. See text for details.

207 The SAL overlap coincidence modules used for forming the pulses that were
208 sent to the FP TDCs and scalers were continuously updating. An output pulse
209 was generated whenever the two input pulses overlapped and was terminated
210 whenever one or both inputs were reset. An overlap of at least 3 ns was neces-
211 sary to produce an output pulse. This behavior is asymmetric to the LRS 622
212 coincidence module used to generate the pFP trigger – it produced a fixed out-
213 put pulse that began when the discriminator output signals from the two FP
214 counters overlapped. The CAEN V775 single-hit TDCs used to instrument the
215 focal plane were experimentally determined to require input pulses of at least
216 11 ns in width in order to register the pulses. In contrast, the CAEN 830 scalers
217 which counted the recoiling electrons were experimentally determined to require
218 input pulses of at least 3 ns in width in order to register the pulses⁵.

219 Figure 10 shows the count rate relative to the trigger rate for FP channel
220 24 for a wide range of relative pulse timings generated by a pulser. In this test,
221 pulser triggers running at 10 Hz were fed into the SAL overlap coincidence unit
222 inputs for the front and back scintillator planes corresponding to FP channel 24.
223 Tests were performed for pulse widths of 25 ns, 35 ns, and 45 ns. The relative
224 timing between the front and back pulses was then varied in steps of a few ns
225 over a total range of ± 40 ns. The open circles correspond to the FP channel 24
226 scaler, while the filled triangles correspond to the FP channel 24 TDC. Clearly,
227 over the entire dynamic range investigated, the CAEN V830 scalers were able to
228 register the signals from the SAL overlap coincidence units. This was true even
229 when the timing of the back-plane pulse relative to the front-plane pulse was
230 artificially fixed 40 ns early or 40 ns late, resulting in an overlap pulse of ~ 3 ns
231 width. On the other hand, the CAEN V775 single-hit TDCs only registered
232 pulses when the timing of the back-plane pulse relative to the front-plane pulse
233 was between 35 ns early and 30 ns late, resulting in an overlap pulse of ~ 11 ns
234 width.

⁵ Note that this ~ 3 ns width is comparable to the smallest pulse that can be generated by the coincidence modules, so that the scalers may register even shorter pulses.

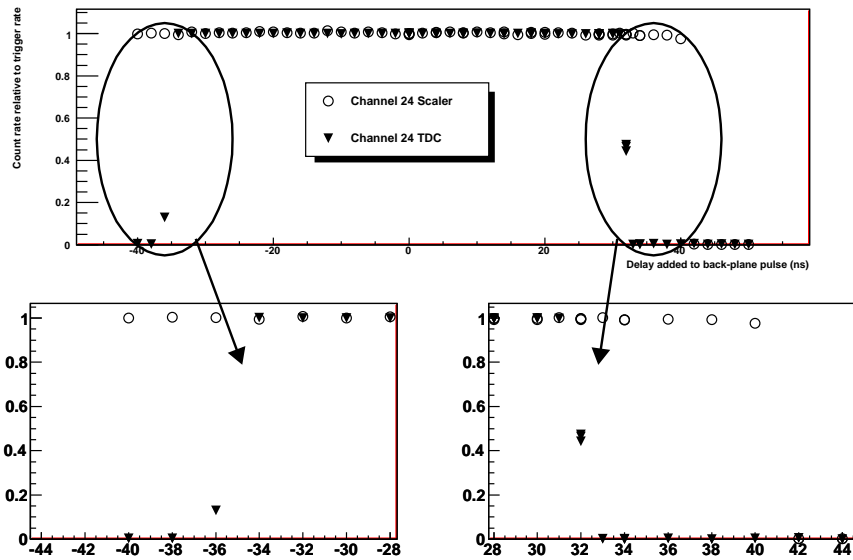


Figure 10: A comparison of the response of FP channel 24 TDCs and scalers when the pulses from the front-scintillator plane and the back-scintillator plane are set to 45 ns in width and the relative timing of the back-plane pulses is then varied by ± 40 ns. Open circles correspond to the scaler and filled triangles correspond to the TDC. The bottom left panel is an enlargement of the top panel from -44 ns to -28 ns and the bottom right panel is an enlargement of the top panel from 28 ns to 44 ns. There is a clear asymmetry in the response of the two modules for shifts in relative timings of more than 30 ns.

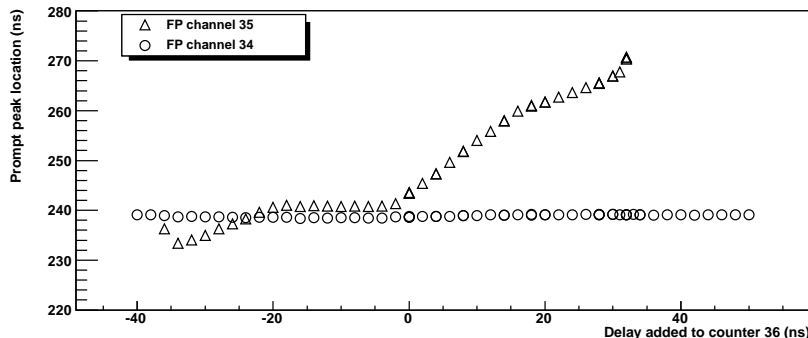


Figure 11: Ghost timing. Recall Fig. 4. The location of the overlap coincidence peak in the FP TDCs for channels 34 and 35 is shown as a function of varying the delay in FP counter 36. See text for details.

235 The fact that a ~ 3 ns overlap pulse could generate a pFP trigger and, conse-
 236 quently, a start signal for the FP TDCs but an ~ 11 ns overlap pulse was needed
 237 to generate a stop signal resulted in missing stops. The flat distribution from
 238 channels 180 to 400 in Fig. 7 thus resulted from random electrons stopping the
 239 FP TDC. Obviously, this important asymmetry in the response of the electron-
 240 ics must be taken into account and corrected in order to properly normalize
 241 experimental data.

242 A peculiar feature of the FP TDCs and/or overlap coincidence modules
 243 was observed during the test of the FP TDC resolving time. This test was
 244 performed using a 10 kHz pulser, and the signal from the pulser was split into
 245 three identical copies, which were then passed to the electronics connected to
 246 FP counters 34 (front plane), 35 (back plane), and 36 (front plane). Holding the
 247 timing fixed for the counter 34 and 35 electronics, it was observed that as delay
 248 was added to or removed from counter 36, the location of the counter 35/36
 249 (channel 34) overlap coincidence peak in the FP TDC varied by as much as
 250 40 ns. A shift was expected to some degree (for example, for fixed counters 34
 251 and 35, as counter 36 is mistimed to arrive later and later, then the coincidence
 252 peak representing counter 35/36 overlaps should also shift in time by the amount
 253 of the mistiming); however, the behavior shown in Fig. 11 is not consistent with

254 this behavior. There is a shift in the prompt peak location at around -30 ns of
 255 added delay as well as non-linear behavior (a “kink” and then a “dogleg”) above
 256 $+20$ ns. This variation in the location of the coincidence peak as a function of
 257 the relative timing of the front-plane and back-plane signals explains the ghost-
 258 peak structure in Fig. 4 (recall the three peaks) and the satellite peak between
 259 channels 150 and 165 in Fig. 7. This effect was included in the simulation.

260 4.2. Electron-beam profile

261 One very important input parameter to the simulation is the time profile of
 262 the electron beam extracted from the PSR. Unfortunately, this is not directly
 263 accessible from the data. To obtain the time profile of the electron beam, the
 264 subset of the data pertaining only to pFP triggers was employed. This data set
 265 was generated by requiring a recoil-electron signal in a specific FP channel. For
 266 this data set, recoil electrons striking FP channels well-separated from the se-
 267 lected channel were taken to be accidentals. The FP TDC distributions for these
 268 distant channels were then summed together to produce a purely accidental FP
 269 TDC spectrum, $A(t)$, with high statistics. This spectrum was then related to
 270 the true electron-beam profile via an auto-correlation function according to

$$A(t) = \int_{-\infty}^{\infty} P(T)P(t+T)dT. \quad (1)$$

271 The method of Fourier transform was then used to extract the beam profile $P(t)$
 272 shown in the top panel of Fig. 12⁶. The secondary and tertiary time structures
 273 in this distribution result from the 3.3 MHz frequency (305 ns period) of the
 274 shaker used in the extraction of the electron beam and the incomplete filling of
 275 the 32.4 m diameter (108 ns period) MAX I PSR.

⁶ An array was created representing the accidental spectrum with one entry per ns. The FFT transform function in ROOT was then used to produce $P^2(T)$. High-frequency terms deemed unimportant were filtered before taking the square root of $P^2(T)$ and performing the inverse FFT.

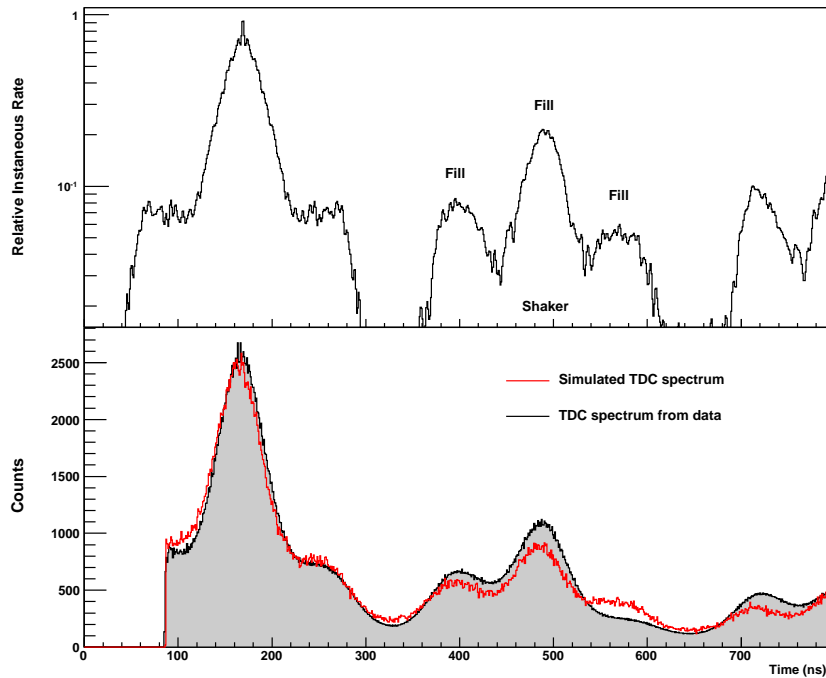


Figure 12: (Color online) (Top panel) The electron-beam time profile, $P(t)$. The observed time structure is due to incomplete filling of the 32.4 m diameter (108 ns) MAX I PSR and the 3.3 MHz frequency (305 ns period) of the extraction shaker. The dropoff between the intensity of the first pulse and the second pulse is roughly a factor of four. This dropoff rapidly vanishes after the second pulse. The profile repeats throughout the 100 ms extraction of the beam. See text for details. (Bottom panel) A comparison between a simulated accidental TDC spectrum, $A(t)$, for the OR of all 62 FP TDCs and data (shaded). The simulation input was the electron-beam profile shown in the top panel together with the parameters presented in Table 1. Agreement is excellent, confirming our understanding of the input parameters.

276 *4.3. Instantaneous electron beam rates*

277 The determination of the average instantaneous beam rate over one beam
278 period (hereafter, the instantaneous rate) is crucial for an accurate calculation
279 of both the stolen coincidences and the ghost corrections. The rate is given by
280 the time constant of the accidental TDC spectrum which can be determined by
281 fitting the data with an exponential function. However, due to the complicated
282 time structure of the beam, the method of extracting the rate must be carefully
283 chosen so as not to be sensitive to the fitting region selected. This is done by
284 defining the fitting function as

$$f(t) = p_0 A(t) e^{-Rt} + p_1 e^{(t-t_0)^2/2\sigma^2}, \quad (2)$$

285 where p_0 and p_1 are constants, $A(t)$ is the FP TDC spectrum for accidental
286 events (see Eq. 1), and R is the instantaneous rate. Since the spectrum also
287 contains some true coincidences, a Gaussian function centered at t_0 is used to
288 account for these events so as to eliminate any bias they might cause in the
289 fitting procedure. As seen in Fig. 13, this method accurately fits the data.

290 **5. Comparison to data**

291 *5.1. Focal-plane TDC spectrum*

292 Figure 12 (bottom panel) shows a comparison between the simulated FP TDC
293 spectrum for accidentals for the OR of all 62 FP TDCs and data. The inputs included
294 the electron-beam profile shown in the top panel of Fig. 12 together with all the
295 parameters presented in Table 1. A correction based on the location of the coincidence
296 peak has been applied to align all of the individual 62 FP TDC spectra. The broad
297 peaks in this spectrum are due to the structures in the electron beam extracted from
298 the PSR. Time periods when greater numbers of electrons are extracted from the
299 PSR correspond to enhancements in the number of tagged photons available to the
300 experiment. The agreement between the data and the simulation is excellent.

301 *5.2. Scaler rates and system deadtime*

302 A rate-dependent study of the effects of deadtime in the FP electronics was per-
303 formed using a standard 45% duty-factor electron beam to determine the impact on

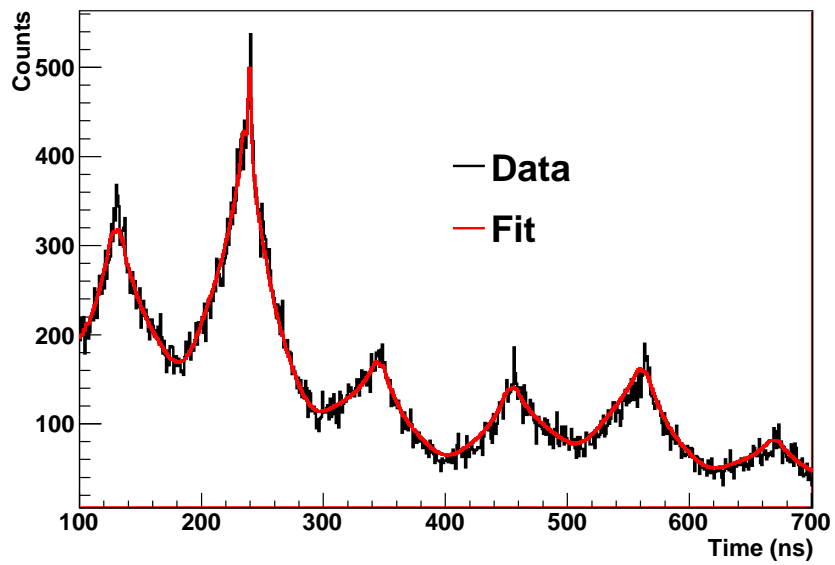


Figure 13: (Color online) The result of fitting Eq. 2 to FP channel 17 TDC data (shown as a histogram). The time constant of the fit is employed in the simulation as the instantaneous electron rate. The true coincidences occur at $t_0 = 240$ ns.

Table 1: Simulation input parameters. See text for details.

Input parameter	Description
total run time	number of ns to run the simulation
electron rate in reference channel	taken from data, ~ 1 MHz
cosmic-ray event rate	taken from data, ~ 50 Hz
untagged event rate	taken from data, ~ 50 – 150 Hz
probability of a tagged event	taken from data, $\sim 50\%$ (inbeam), $\sim 0.5\%$ (scattering)
electron rate relative to reference channel	taken from data, ~ 1 – 4
focal-plane discriminator pulse width	leading edge, ~ 25 – 50 ns
inhibit duration	bad beam or DAQ busy, ~ 1 ms
geometric double	recoil electron strikes adjacent channels, $\sim 1\%$
pFP trigger channel	channel 32
pFP trigger pulse width	same as focal-plane discriminator pulse width, ~ 25 – 50 ns
pFP overlap properties	flag, module (non)updating
pFP trigger	flag, on/off
duty-factor meter (DFM) counters	counter 20 and counter 50
DFM pulse widths	~ 25 – 50 ns
DFM overlap characteristics	flag, module (non)updating
prompt-peak location	Δt between FP TDC start and prompt peak, ~ 100 ns
periodicity of the electron-beam profile	long enough to generate several repetitions
electron-beam profile	see top panel of Fig. 12

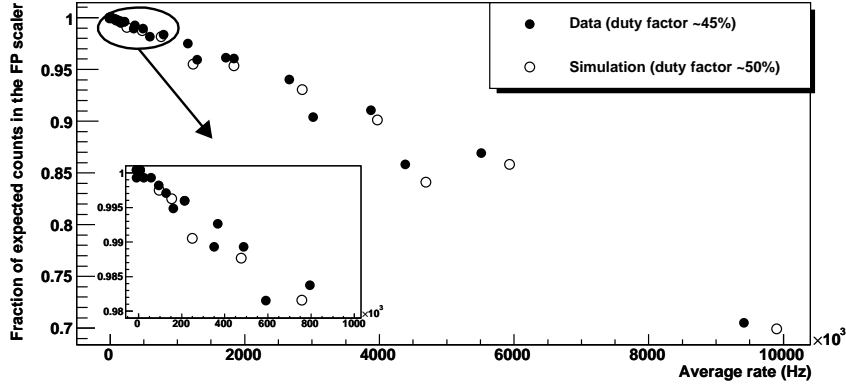


Figure 14: Recoil-electron loss effects. A comparison between data (filled circles) and simulation (open symbols) of the fraction of post-bremsstrahlung electrons counted by the FP scalers as a function of average recoil-electron rate. The inset expands the region up to 1 MHz. See text for details.

304 the FP scalers. FP channels 5, 15, 25, and 35 were first tested individually, then OR-
 305 ed together in two groups of two (5 and 15, 25 and 35), and finally tested as a single
 306 group of four in order to conveniently increase the available rates. The counts in the
 307 individual channels were used to determine the actual numbers of counts reaching the
 308 FP scalers. The fraction of counts reaching the FP scalers for the twofold and fourfold
 309 ORs was then monitored as a function of rate. Figure 14 shows data (solid circles) for
 310 the fraction of expected counts in the twofold and fourfold configurations as a function
 311 of average recoil-electron rate. Simulated values are shown for a duty factor of about
 312 50% (open circles). The inset shows the densely populated region from 0 to 1 MHz.
 313 Clearly, the simulation does an excellent job of predicting the loss of counts in the FP
 314 scalers due to deadtime effects.

315 5.3. Prescaled focal-plane trigger

316 It is straightforward to compare the data collected using the pFP trigger to the
 317 simulation because the trigger source is one of the FP channels. The number of stolen
 318 coincidences in the pFP trigger channel is the ratio of the number of counts in the
 319 TDC prompt peak (recall Fig. 7) to the total number of triggers. Since events with
 320 an output width of less than 11 ns in the coincidence overlap module do not register

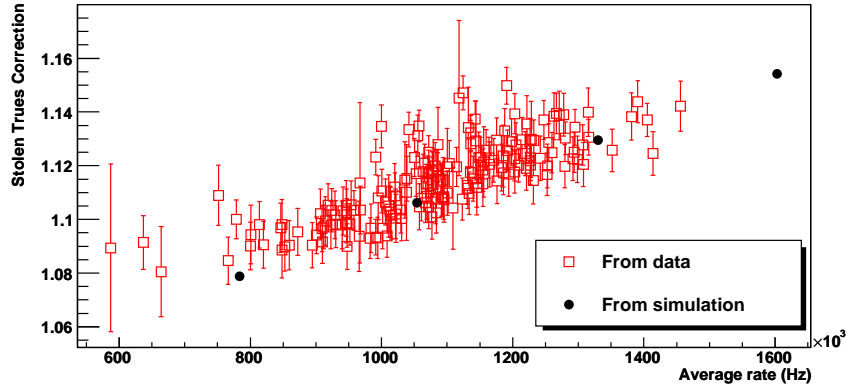


Figure 15: (Color online) A comparison between the stolen-coincidences corrections for the pFP trigger obtained from the data (open squares) and the simulation (filled circles).

321 a stop in the FP TDCs, it is important to include events to the right of the prompt
 322 peak as stolen coincidences since these events were not recorded due to the limitations
 323 in the electronics setup. Using data, the stolen coincidences can be determined for the
 324 pFP trigger on a run-by-run basis (recall Fig. 7). The stolen coincidences can also be
 325 calculated using the simulation at several recoil-electron rates. A comparison of the
 326 two approaches is presented in Fig. 15.

327 5.4. Stolen-coincidence correction

328 A method for analytically calculating the stolen coincidences for a nearly contin-
 329 uous beam is given in Ref. [15]. The stolen-coincidence correction is given by

$$f_{\text{stolen}} = e^{R\tau}, \quad (3)$$

330 where R is the electron rate and τ is the time between the start of the TDC and the
 331 arrival of the corresponding tagged electrons. The stolen-coincidence correction can
 332 also be determined via the simulation. The simulated, tagged-photon TDC spectrum
 333 (see Fig. 16) shows both prompt events and stolen coincidences. The fraction of stolen
 334 coincidences determined using the simulated tagged photons is given by

$$f_{\text{stolen}}^{\text{sim,tag}} = \frac{N}{N_{\text{prompt}}}, \quad (4)$$

Table 2: Comparison of the fraction of stolen coincidences obtained using Eq. 3 and the simulation.

Rate _{inst} /MHz	τ /ns	$f_{\text{stolen}}^{\text{calculated}}$	$f_{\text{stolen}}^{\text{simulated}}$
1.0	19	1.019	1.018 ± 0.001
2.0	19	1.039	1.036 ± 0.001
1.0	199	1.220	1.211 ± 0.001
2.0	199	1.489	1.477 ± 0.002

where N is the total number of events and N_{prompt} is the number of events arriving during the prompt window.

Several values of R and τ were chosen as simulation inputs in order to compare the simulated stolen coincidences to those predicted by Eq. 3. The results are shown in Table 2. Agreement is excellent.

Another method [16] for determining the stolen-coincidence correction determines the correction from the accidental FP TDC spectrum [16] (see Fig. 16). With this approach, the correction factor is given by

$$f_{\text{stolen}}^{\text{accidentals}} = \frac{N}{N - N_{t < t_{\text{left}}}}, \quad (5)$$

where N is the total number of events and $N_{t < t_{\text{left}}}$ is the number of events arriving prior to the coincidence peak (located at t_0). The stolen-coincidence correction was calculated for both a simulated accidental FP TDC spectrum and the TDC spectrum of the tagged photons. The results are shown in Table 3. Agreement is excellent.

5.5. Ghosts correction

The correction for the rate-dependent ghost effect differs from the stolen-coincidence correction in that an exact analytical form for the correction does not exist. However, it is possible to compare the results of the simulation to the values used by Hornidge *et al.* [12, 13]. Unfortunately, it is impossible to replicate the exact parameters of the SAL configuration. Additionally, the results given by Hornidge *et al.* are run-averaged results. Still, a comparison of the ghost corrections is useful in evaluating the overall accuracy of our FP simulation.

Table 3: Comparison of the of the stolen-coincidence correction obtained using Eq. 5 applied to the accidental TDC spectrum and Eq. 4 applied to the tagged photons TDC spectrum.

FP ch	$f_{\text{stolen}}^{\text{accidentals}}$	$f_{\text{stolen}}^{\text{tagged}}$
0	1.521	1.519
10	1.567	1.578
20	1.672	1.670
30	1.739	1.738
40	1.768	1.785
50	1.900	1.916
60	2.029	2.056

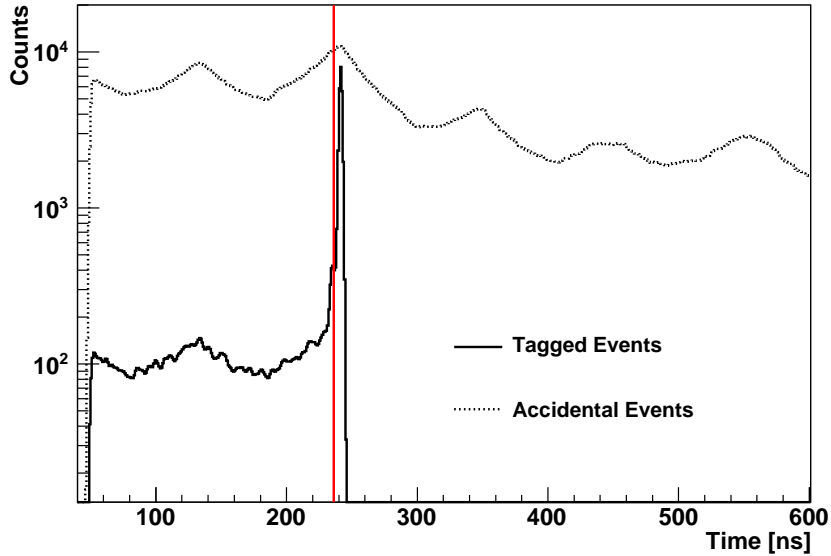


Figure 16: (Color online) Spectra for FP channel 30 used to obtain the stolen-coincidence correction via Eq. 5. The lower solid spectrum corresponds to the tagged-photon TDC, while the upper dotted spectrum is simulated accidentals. The prompt peak is located at $t_0 = 240$ ns. Stolen coincidences appear to the left of this peak. The red line indicates the location of t_{left} . See text for details.

Table 4: Comparison of the ghost correction obtained in Ref [12] and our simulation.

Rate _{inst} /MHz	$f_{\text{ghosts}}^{\text{Hornidge}}$	$f_{\text{ghosts}}^{\text{this work}}$
1.400	1.019	0.993
4.755	1.076	1.007

355 In order to perform such a comparison, the beam conditions were reconstructed
 356 as carefully as possible to best reproduce the conditions of the SAL experiment.
 357 The beam rates (1.4 and 4.755 MHz) were chosen to match two of those listed by
 358 Hornidge *et al.* The ghost correction is defined as

$$1/f_{\text{ghost}} = \sigma_M/\sigma, \tag{6}$$

359 where σ_M is the measured cross section and σ is the real cross section. The correc-
 360 tion factors predicted by the FP simulation are compared to the values obtained by
 361 Hornidge *et al.* in Table 4. The apparent disagreement in these results is likely due to
 362 undocumented differences in the two experimental setups (for example: discriminator
 363 modes, pulse timing, TDC behavior, and beam structure). It is probably impossible
 364 to improve the agreement without completely recreating the precise conditions of the
 365 SAL experiment.

366 5.6. Systematic Uncertainties

367 The systematic uncertainties in the ghosts and stolen-coincidence corrections was
 368 determined as a function of variations in (1) the FP discriminator pulse width, (2) the
 369 time profile of the stretched electron beam leaving the PSR, and (3) the electron rate
 370 in the individual FP channels.

371 During the inaugural run periods at the TPF, the FP discriminator pulse widths
 372 were typically set to (50 ± 1) ns⁷. In the simulation, the discriminator pulse widths
 373 were varied by ± 2 ns to see how the corrections were affected. In this case, both the
 374 stolen-coincidence and ghosts correction varied by less than 0.5%.

⁷ Today, the FP discriminator pulse widths are typically set to (25 ± 1) ns.

Table 5: Systematic uncertainties in the stolen-coincidence and ghosts corrections due to simulation parameter variations.

varied parameter	effect on correction	
	stolen coincidences	ghosts
FP discriminator pulse width	0.5%	0.5%
time profile of the extracted electron beam	2%	3%
electron rate in FP channels	5% (see text)	1%

375 Understanding the effect of the time profile of the beam on the corrections was more
376 involved. Conceptually, the electron-beam profile after the PSR could be more uniform
377 (“flatter” as a function of time representing a more continuous beam) or less uniform
378 (higher peaks and lower valleys as a function of time representing a less continuous
379 beam) than the profile used. To obtain a more uniform time profile, $[P(t)]^{0.75}$ was
380 employed; the less uniform profile was given by $[P(t)]^{1.33}$. Exponents smaller than
381 0.75 or larger than 1.33 resulted in simulated accidental TDC spectra that did not
382 reproduce the data. The variation in the stolen-coincidence correction due to these
383 extreme profiles was less than 2%. The variation of the ghosts correction was less than
384 3%.

385 The stolen-coincidence correction depends on the electron rate according to Eq. 3.
386 Further, a rate-independent method to extract the correction is presented in Eq. 4. The
387 difference between these methods is typically 2% or less. Using Eq. 3 and assuming the
388 electron rate varies by $\sim 10\%$, the correction is found to have a systematic uncertainty
389 of $\leq 5\%$. Combining these results, the variation of the stolen-coincidence correction
390 as a function of electron rate is taken to be 5%. The effect of the electron rate on the
391 ghosts correction was investigated by varying the nominal electron beam rate during
392 in the simulation by $\pm 25\%$. The ghost correction varied by less than 1% over this
393 range of beam rates.

394 A summary of the systematic uncertainties in the stolen-coincidence and ghosts
395 corrections due to simulation parameter variations is presented in Table 5.

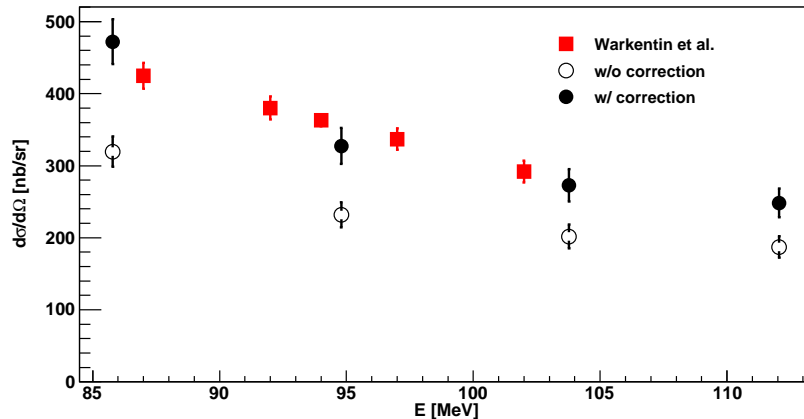


Figure 17: (Color online) Absolute differential cross-section data corrected for rate-dependent effects as outlined in this paper compared to published data. Statistical uncertainties only are shown. See text for details.

396 5.7. Carbon elastic scattering cross section for photons

397 As an illustration of the success of our Monte Carlo method for addressing rate-
 398 dependent effects, Fig. 17 presents a comparison between the absolute differential cross
 399 section recently obtained at the TPF at the MAX IV Laboratory and existing data
 400 published by Warkentin *et al.* [18] (filled squares) for elastic photon scattering from ^{12}C
 401 at a lab angle of 60° performed at SAL. Error bars reflect statistical uncertainties only.
 402 The open circles show our cross-section data prior to correction for rate-dependent
 403 effects, while the filled circles show the same data after correction for rate-dependent
 404 effects. The agreement between the two data sets is excellent. A summary of the
 405 rate-dependent corrections is presented in Table 6.

406 6. Summary

407 Rate-dependent effects in the electronics used to instrument the tagger focal plane
 408 at the Tagged-Photon Facility at the MAX IV Laboratory have been investigated using
 409 a dedicated Monte Carlo simulation. The Monte Carlo simulation incorporates the
 410 unique behaviors of each of the critical focal-plane instrumentation modules. Results
 411 have been compared to analytical calculations of these effects, as well as experimental
 412 data collected for a series of specialized tests of the rate-dependent response. The

Table 6: Stolen-coincidence and ghosts corrections applied to the ^{12}C data shown in Fig. 17. Non-negligible statistical uncertainties are listed.

photon energy / MeV	86	95	104	112
Uncorrected Cross Section / nb/sr	320 ± 21	232 ± 17	202 ± 16	187 ± 15
Stolen Trues Correction	1.49	1.43	1.37	1.33
Ghosts Correction	0.99	0.99	0.99	1.00
Corrected Cross Section / nb/sr	472 ± 31	327 ± 25	273 ± 22	248 ± 20

413 simulation agrees very well with both. Further, the output of the simulation has been
 414 used to normalize high-rate tagged-photon production data (1 MHz average and up
 415 to 4 MHz instantaneous rates per focal-plane channel). Rate-corrected cross-section
 416 data are in excellent agreement with previous results obtained at lower instantaneous
 417 rates. We assert that this Monte Carlo simulation is of fundamental importance to
 418 the analysis of all experimental data from the Tagged-Photon Facility at the MAX IV
 419 Laboratory and, in principle, is adaptable to any high-rate coincidence experiment.

420 Acknowledgements

421 This project was supported by the US National Science Foundation Grant No.
 422 0855569, as well as The Swedish Research Council, the Crafoord Foundation, and the
 423 Royal Physiographic Society in Lund. The authors gratefully acknowledge the Data
 424 Management and Software Centre, a Danish Contribution to the European Spallation
 425 Source ESS AB, for generously providing access to their computations cluster.

426 References

- 427 [1] <https://www.maxlab.lu.se>
- 428 [2] J.-O. Adler, M. Boland, J. Brudvik, K. Fissum, K. Hansen, L. Isaksson, P. Lilja,
 429 L.-J. Lindgren, M. Lundin, B. Nilsson, D. Pugachov, A. Sandell, B. Schröder,
 430 V. Avdeichikov, P. Golubev, B. Jakobsson, J.R.M. Annand, K. Livingston,

- 431 R. Igarashi, L. Myers, A. Nathan, W.J. Briscoe, G. Feldman, M. Kovash, D. Bran-
432 ford, K. Föhl, P. Grabmayr, V. Takau, G. O’Rielly, D. Burdeynyi, V. Ganenko,
433 V. Morochovskyi, G. Vashchenko, Nucl. Instrum. and Meth. A 715 (2013) 1.
- 434 [3] <https://www.maxlab.lu.se/node/1090>
- 435 [4] L.-J. Lindgren, Nucl. Instrum. and Meth. A 492 (2002) 299.
- 436 [5] J.M. Vogt, R.E. Pywell, D.M. Skopik, E.L. Hallin, J.C. Bergstrom, H.S. Caplan,
437 K.I. Blomqvist, W. Del Bianco, J.W. Jury Nucl. Instrum. and Meth. A 324 (1993)
438 198.
- 439 [6] Annual Report 1994, Saskatchewan Accelerator Laboratory, p. 21-23.
- 440 [7] Annual Report 1995, Saskatchewan Accelerator Laboratory, p. 27-29.
- 441 [8] see for example J.-O. Adler, B.-E. Andersson, K.I. Blomqvist, B. Forkman,
442 K. Hansen, L. Isaksson, K. Lindgren, D. Nilsson, A. Sandell, B. Schröder, K. Zi-
443 akas, Nucl. Instr. and Meth. A 294 (1990) 15.
- 444 [9] see for example J.-O. Adler, B.-E. Andersson, K.I. Blomqvist, K.G. Fissum,
445 K. Hansen, L. Isaksson, B. Nilsson, D. Nilsson, H. Ruijter, A. Sandell, B. Schröder,
446 D.A. Sims, Nucl. Instr. and Meth. A 388 (1997) 17.
- 447 [10] J.M. Vogt, R. Florizone, Nucl. Instr. and Meth. A 339 (1994) 425.
- 448 [11] L.S. Myers, PhD thesis, University of Illinois at
449 Urbana-Champaign, USA (2010) unpublished; see also
450 <https://www.maxlab.lu.se/sites/default/files/myers.pdf>
- 451 [12] D.L. Hornidge, PhD thesis, University of Saskatchewan, Canada (1999) unpub-
452 lished; see also http://www.mta.ca/~dhornidg/hornidge_phd.pdf
- 453 [13] D.L. Hornidge, B.J. Warkentin, R. Igarashi, J.C. Bergstrom, E.L. Hallin,
454 N.R. Kolb, R.E. Pywell, D.M. Skopik, J.M. Vogt Phys. Rev. Lett. 84 (2000)
455 2334.
- 456 [14] R.E. Pywell, Subatomic Physics Internal Reports, Univer-
457 sity of Saskatchewan, Canada (2009) unpublished; see also
458 http://nucleus.usask.ca/technical_reports/other/TaggerSim-1.1.pdf

- 459 [15] R.O. Owens, Nucl. Instr. and Meth. A 288 (1990) 574.
- 460 [16] L. Van Hoorebeke, D. Ryckbosch, C. Van den Abeele, R. Van de Vyver, J. Dias,
461 F. De Smet, B. Schröder, D. Nilsson Nucl. Instr. and Meth. A 321 (1992) 230.
- 462 [17] <http://root.cern.ch>
- 463 [18] B.J. Warkentin, D.L. Hornidge, R. Igarashi, J.C. Bergstrom, E.L. Hallin,
464 N.R. Kolb, R.E. Pywell, D.M. Skopik, J.M. Vogt, G. Feldman Phys. Rev. C
465 64 (2001) 014603.